

Article

Corrosion Behavior of a Cr-Al Coating Deposited on 304 Austenitic Stainless Steel by Multi-Arc Ion Plating in Liquid Lead–Bismuth Eutectic

Weijian Sun ¹, Zhenghua Tang ^{1,*}, Jun Wang ², Guang Chen ², Wen Yang ¹ and Haibo Zhao ³

¹ School of Material Science and Engineering, Sichuan University, Chengdu 610065, China; sunweijian@stu.scu.edu.cn (W.S.); 2019223015082@stu.scu.edu.cn (W.Y.)

² School of Mechanical Engineering, Sichuan University, Chengdu 610065, China; srwangjun@scu.edu.cn (J.W.); scuchenkevin@163.com (G.C.)

³ Analytical & Testing Center, Sichuan University, Chengdu 610065, China; zhaohaibocd@sohu.com

* Correspondence: sacdtzh@163.com

Abstract: In this paper, a Cr-Al coating was deposited using multi-arc ion plating (MAIP) on 304 austenitic stainless steel. The Cr-Al-coated sample was treated by vacuum annealing at 600 °C for 12 h, and its corrosion behaviors against static LBE were carefully evaluated by SEM, EDS and XPS at a temperature of 600 °C for 1000 h, compared with an uncoated sample. The results showed that the uncoated sample was corroded by the dissolution and oxidation of LBE severely; a duplex-layered oxide layer consisting of an outer Fe₃O₄ magnetite layer and an inner FeCr₂O₄ spinel layer was produced on the surface of 304 stainless steel after LBE corrosion. For Cr-Al diffusion coating, an oxide layer was formed that separated the LBE into the 304 matrix. XPS detection showed that the oxide layer primarily included Al₂O₃. Besides this, the hardness of the coating was tested with a Vickers hardness tester, and the annealed Cr-Al diffusion coating exhibited an average hardness of 260 HV, about five times as high as the Al coating before annealing, of which the average hardness was 48 HV.

Keywords: 304 austenitic stainless steel; multi-arc ion plating Cr-Al coating; oxide layer; lead–bismuth eutectic



Citation: Sun, W.; Tang, Z.; Wang, J.; Chen, G.; Yang, W.; Zhao, H. Corrosion Behavior of a Cr-Al Coating Deposited on 304 Austenitic Stainless Steel by Multi-Arc Ion Plating in Liquid Lead–Bismuth Eutectic. *Coatings* **2022**, *12*, 667. <https://doi.org/10.3390/coatings12050667>

Received: 28 March 2022

Accepted: 11 May 2022

Published: 13 May 2022

Publisher's Note: MDPI stays neutral with regard to jurisdictional claims in published maps and institutional affiliations.



Copyright: © 2022 by the authors. Licensee MDPI, Basel, Switzerland. This article is an open access article distributed under the terms and conditions of the Creative Commons Attribution (CC BY) license (<https://creativecommons.org/licenses/by/4.0/>).

1. Introduction

Nowadays, among the nuclear power plants in the world, the most widely used is the fast neutron reactor. In fast reactors, liquid lead–bismuth eutectic alloy (LBE) has good thermo-physical properties, neutron economics and high chemical inertness, such that LBE has become one of several types of candidate material for coolants in fast neutron reactors [1–5]. LBE, however, at high temperatures has a strong corrosive effect on structural materials during the operation of the fast neutron reactor [6]. The component elements—such as Fe, Cr and Ni—contained in the metal structural materials will dissolve in the LBE, and the impurity of the oxygen in the LBE will interact with the solid [7]. The chemical reaction of the material component elements leads to material failure. At the same time, the material embrittlement effect induced by Pb and Bi, namely the embrittlement effect of liquid metal (LME, Liquid Metal Embrittlement [8–10]) is also a certain destructive corrosion type.

Austenitic stainless steel has long been considered the perfect choice for high temperature applications. This is not only because of its mechanical stability but also because of its excellent corrosion resistance and oxidation resistance in many applications, such as AISI 304H stainless steel and 304 stainless steel [11–13]. Thus, 304 stainless steel can be the candidate structural material for LBE-cooled fast neutron reactor applications. Because corrosion attack in LBE is a key issue that restricts the development of nuclear reactors, it is

also necessary to find a good way to protect the structural materials, and coating technology is one of the most effective technologies to solve the corrosion of structural materials.

At present, ceramic coatings such as oxides or nitrides, and aluminide coatings are widely used [14,15]. In particular, aluminum has the strongest affinity with oxygen, and can preferentially combine with oxygen in LBE to form stable and compact oxides. The aluminum element is selectively oxidized on the surface by diffusion to form a layer of Al_2O_3 protective film [16]. Garcia Ferre et al. [17] proposed an Al_2O_3 coating, which was produced via pulsed laser deposition. The results showed that the coatings protected substrates working in heavy liquid metals (HLMS) at high temperatures. Miorin et al. [18] investigated two different aluminum-rich layers: Al_2O_3 coating and TiAlN film, which were grown via radio frequency magnetron sputtering and high power impulse magnetron sputtering, respectively. Both types of coatings proved to be effective in protecting the substrate in stagnant Pb at 550 °C for 1200 h. Moreover, Wu et al. [19] synthesized an AlTiN coating on a 316 L stainless steel substrate via cathodic arc ion plating, and LBE corroded it at 550 °C and 600 °C for 500 h. The results showed that the coating can effectively improve the LBE corrosion resistance of a 316 L stainless steel substrate at 550 °C and 600 °C. According to a previous study, adding alloying elements to the aluminide coating can further improve the corrosion resistance of the coating. Charalampopoulou et al. [20] used magnetron sputtering to prepare Cr_2AlC coatings on the surface of austenitic stainless steels. Their thickness was about 3 μm . After 1000 h of corrosion in 500 °C LBE, the coating did not undergo visible oxidation or dissolution corrosion, because the melting point of Cr is as high as 1857 °C, and Cr has good thermal corrosion resistance. Meanwhile, the incorporation of Cr can promote the formation of an oxide layer [21–25]. Simultaneously, we should consider that LBE in a nuclear reactor is flowing under the actual working conditions, and the flowing liquid metal will cause erosion and abrasion to the structural materials. The addition of Cr can increase the hardness and wear resistance of the coating in another aspect [26–28].

Multi-arc ion plating (MAIP) has the advantages of a rapid deposition rate, good wrapping properties, a smooth surface of the deposited coating, a compact structure, good mechanical properties, and good bonding performance with the substrate [29]. Therefore, MAIP technology is widely used in a wide range of applications.

The previous studies paid much less attention to a Cr-Al coating on the corrosion of LBE. Therefore, in this paper, a Cr-Al coating on austenitic stainless steel 304 was fabricated by MAIP Cr and MAIP Al. The corrosion behaviors of an uncoated sample and the Cr-Al-coated sample against static LBE were carefully investigated at 600 °C for 1000 h. The purpose of this study is to develop a potential corrosion-resistant coating for LBE-cooled fast reactor applications.

2. Materials and Methods

2.1. Coating Preparation

Figure 1 shows the shortened process employed in this work. The chemical compositions (wt.%) of stainless steel 304 used in the corrosion tests are given in Table 1. The Cr-Al coating was deposited on tubes of 304 steel with the diameter of 10 mm, a length of 20 mm, and a thickness of 1 mm. The pristine samples were ultrasonically pre-cleaned in alcohol for 10 min, rinsed with deionized water, and blown dry with nitrogen gas before MAIP.

Table 1. Chemical compositions of stainless steel 304 (wt.%).

C	S	Si	Mn	Ni	Cr	P	Fe
0.035	0.020	0.436	1.100	8.010	18.640	0.013	Bal.

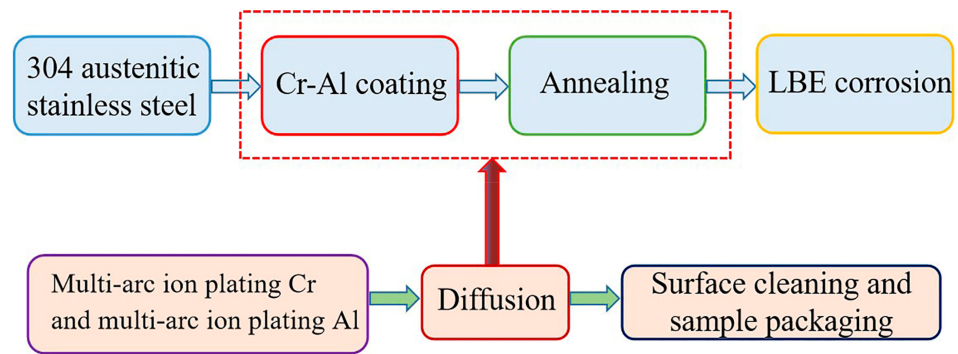


Figure 1. Shortened process in this work.

Cr and Al targets (99 at.% in purity) were used for the deposition. The Cr-Al coating was prepared using a multi-arc ion plating system (provided by Chengdu Qi Xing Vacuum Coating Technology Co., Ltd., Chengdu, China), which is only equipped with one target, as shown in Figure 2. Therefore, aluminum was then deposited after depositing chromium. Prior to the coating deposition [30], the chamber was pumped down to 4×10^{-3} Pa, and was then heated up to 300 °C (for the depositing chromium) and 250 °C (for depositing aluminum) respectively. When the heating temperature and the required vacuum degree are reached, they can be adjusted such that there is an argon gas flow to the ionization vacuum degree of 0.8 Pa, the bias voltage power supply is 400 V, and the arc power supply is 80 A (for depositing chromium) and 60 A (for depositing aluminum) separately. After bombardment for 3 min, the bias voltage was reduced to 100 V, and we started coating. The deposition times of the Cr and Al layers were 4 and 3 h, respectively. The deposition parameters are summarized in Table 2.

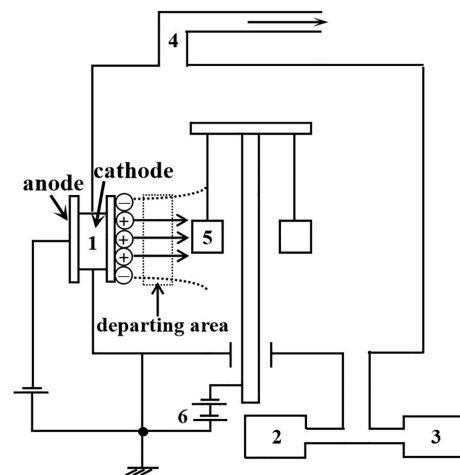


Figure 2. Structure diagram of the multi-arc ion plating equipment: (1) cathodic arc source; (2,3) air intake; (4) vacuum system; (5) samples.

Table 2. Detailed deposition parameters of the Cr-Al coating.

	MAIP Cr	MAIP Al
Substrate Bias voltage (V)	100	100
Working gas	Ar	Ar
Working pressure (Pa)	0.8	1.0
Substrate temperature (°C)	300	250
Target current (A)	80	60
Deposition time (min)	240	180

After the multi-arc ion plating of Al was completed, the sample was put into a resistance furnace, which was placed in a QX-1900 Double Station Vacuum Glove Box (provided by Chengdu Qi Xing Vacuum Coating Technology Co., Ltd.) for vacuum annealing treatment at a temperature of 600 °C for 12 h.

2.2. Corrosion Test

The uncoated sample and the annealed Cr-Al-coated sample were tested in the static LBE at 600 °C for 1000 h. The chemical compositions of LBE with the melting point of 398 K used in this study were 55.5 wt.% Pb and 44.5 wt.% Bi.

The corrosion tests were carried out in a muffle furnace. The samples and the lead–bismuth alloy were placed in a quartz tube, and the vacuum in the quartz tube was pumped to 1.4×10^{-2} Pa. The designed quartz tube is shown in Figure 3. The inner and outer diameters of the tube are, respectively, 21 mm and 26 mm. Because the density of LBE is greater than that of the sample, a neck was fabricated at the $\frac{1}{4}$ -mark of the tube in order to avoid the samples floating on the LBE solution [31]. Before heating, the samples were packed into the short part of the tube, while the solid LBE was put in the long part of the tube. When heated, the solid LBE can melt and immerse the samples.

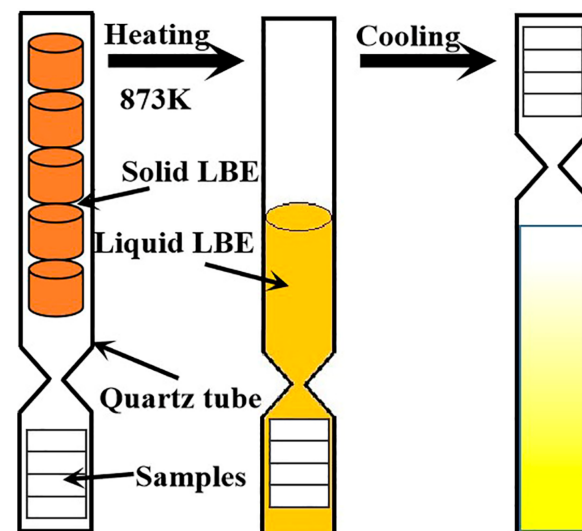


Figure 3. The designed quartz tube and the process of LBE corrosion.

2.3. Coating Characterizations

When the corrosion time in LBE reached 1000 h, we took the samples out of the LBE and prepared them for post-corrosion analysis. For the analysis of the cross-section of the coating, hand grinding was performed on the surface of the samples before and after LBE corrosion with 500-grit, 1000-grit, 1500-grit, and 2000-grit water-abrasive papers, followed by polishing to a 1- μ m diamond finish. For the analysis of the surface of the coating after LBE corrosion, a 1:1:1 solution of hydrogen peroxide, acetic acid and ethanol was used to remove the pre-existing LBE on the surface of the samples [32]. The samples were washed in ethanol, dried, and characterized by Scanning Electron Microscope (SEM), Energy Dispersive Spectroscopy (EDS), Grazing Incident X-ray Diffraction (GIXRD), and X-ray Photoelectric Spectroscopy (XPS). Meanwhile, the hardness of the Cr-Al-coated sample before and after annealing was tested under a Vickers hardness tester with a normal load of 0.245 N.

3. Results and Discussion

3.1. Microstructure Characterization of the Cr-Al Coating before Corrosion

Figure 4a,b shows the cross-sectional SEM image of the Cr-Al coating before and after annealing on stainless steel 304. The thickness of the outer Al layer in Figure 4a was 10.8 μ m.

The thickness of inner Cr layer was 8.7 μm . The whole MAIP Cr-Al coating had a thickness of about 23 μm after annealing; as shown in Figure 4b, it exhibited a dense structure. The MAIP Cr-Al coating was relatively flat and dense, with a uniform thickness and no obvious holes, which can be beneficial to enhancing the corrosion resistance of the coating.

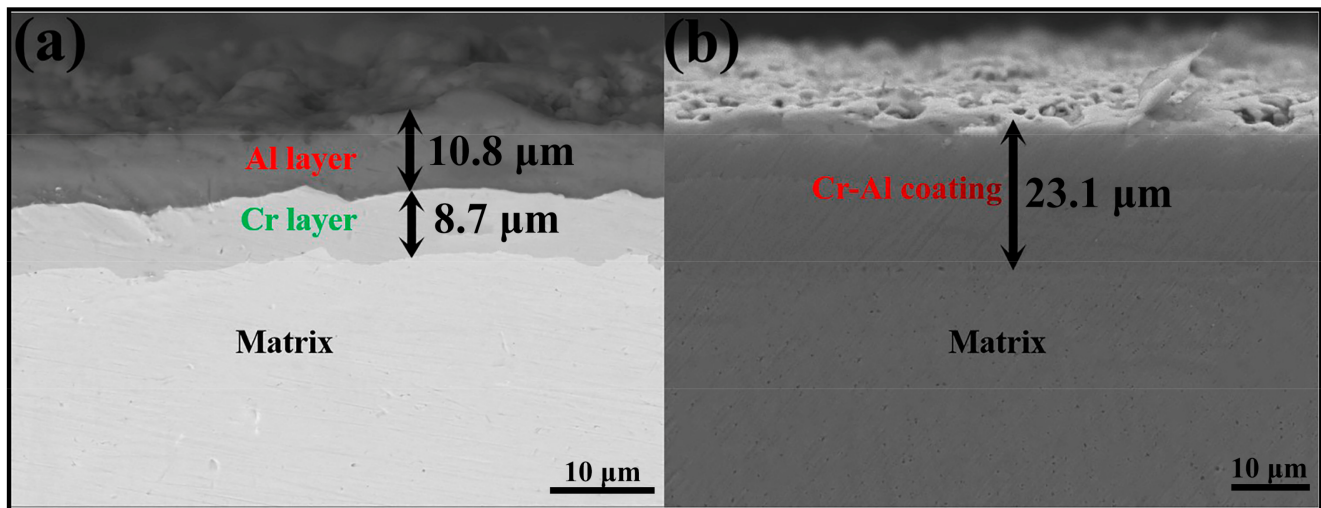


Figure 4. Cross-sectional SEM image of the Cr-Al coating (a) before and (b) after annealing.

The addition of Cr can significantly promote the diffusion process of Al. Due to the densification of the coating caused by the mutual diffusion of Cr and Al, the corrosion resistance of the annealed coating can be effectively improved [26]. Figure 5a shows a cross-sectional SEM image of the Cr-Al diffusion coating. EDS line scans in the matrix-to-coating direction (Figure 5b) show that the mutual diffusion of Cr and Al at 600 °C for 12 h resulted in a single coating composition deviating from the compositional domain for the formation of the Cr-Al phase in the outer MAIP Al layer. Meanwhile, the Fe-Cr-Al diffusion layer appeared between the Al coating and substrates because Fe diffused to the Cr layer further. In order to further investigate the microstructure of the Cr-Al coating after the annealing treatment, EDS was used to analyze the atomic percentage of corresponding area in Figure 5a. The results are shown in Figure 5c,d. The chemical elements at point c are Cr and Al, and their atomic percentages are 55.32% and 44.68%, respectively. The chemical composition (in at.%) of point d is 41.47% Al, 46.11% Cr, and 12.42% Fe. Therefore, the annealed Cr-Al coating was composed of the surface Cr-Al layer and the inner Fe-Cr-Al layer.

In order to further explore the phase structure on the surface of the Cr-Al diffusion coating, GIXRD analysis was performed on the coating surface. The analysis result of the GIXRD is shown in Figure 6. It can be seen that the phase on the surface of the Cr-Al diffusion coating mainly included Al_8Cr_5 .

The Vickers hardness in the coating-to-matrix direction of the Cr-Al-coated sample before and after annealing is shown in Figure 7a. For the same depth, we chose three different points to test the Vickers hardness, and took the average value of the three points as the hardness of the depth. The test points of the Vickers hardness are shown in Figure 7b. Before annealing, the outer Al layer was relatively soft, and its average hardness was about 48 HV. After 12 h of annealing treatment at 600 °C, the hardness of the outer Al layer which had been converted to a Cr-Al layer exhibited an average hardness of 260 HV, which is about five times as high as that of the Al coating before annealing. Simultaneously, the hardness of the matrix remained at about 275 HV. This means that the annealing treatment at 600 °C for 12 h will not have significant influence on the properties of the 304 matrix.

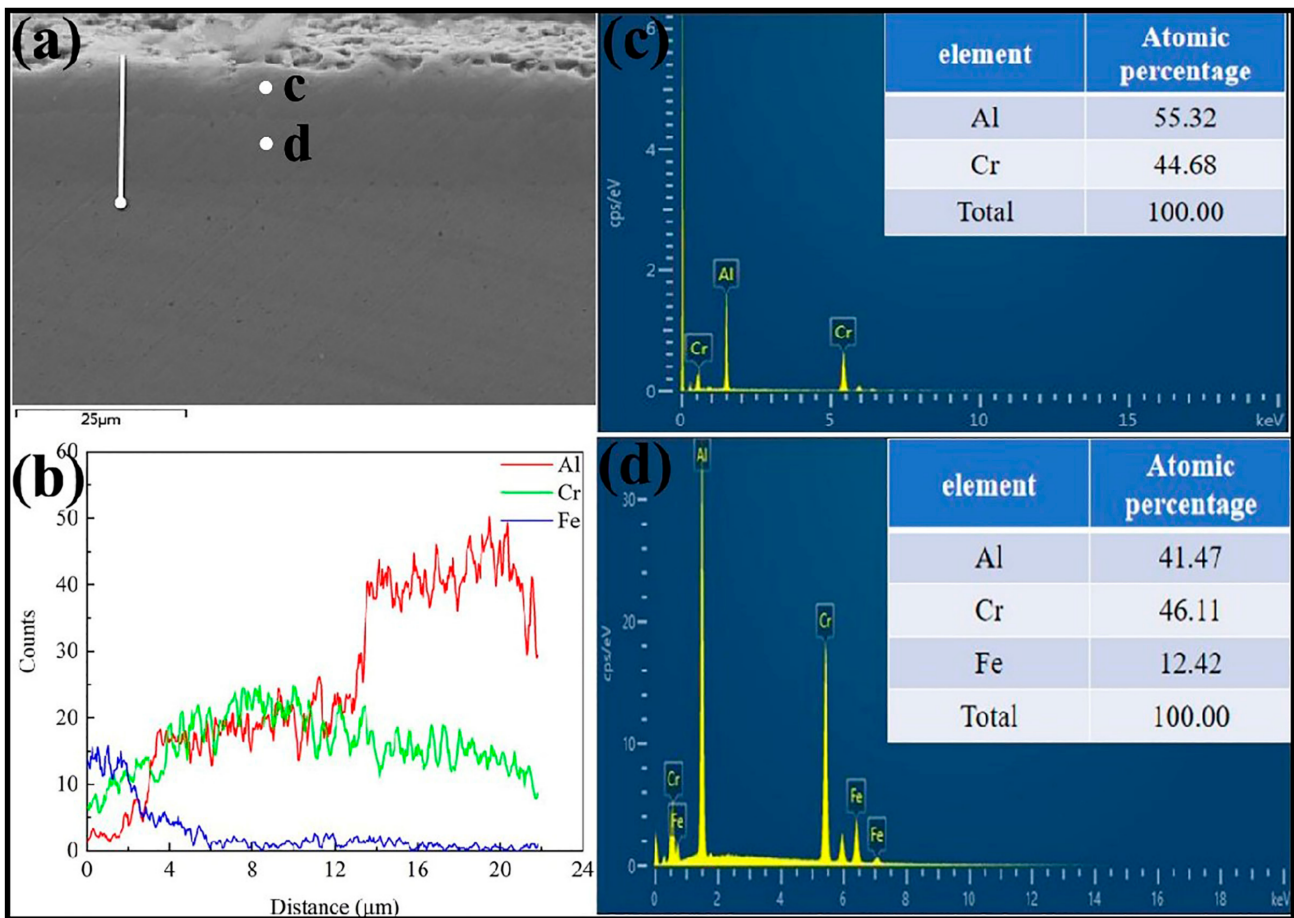


Figure 5. (a) Cross-sectional SEM image of the Cr-Al diffusion coating; (b) SEM-EDS line scans of the Cr-Al diffusion coating; (c,d) SEM-EDS results of the chemical compositions (at.%) of the marked regions in (a).

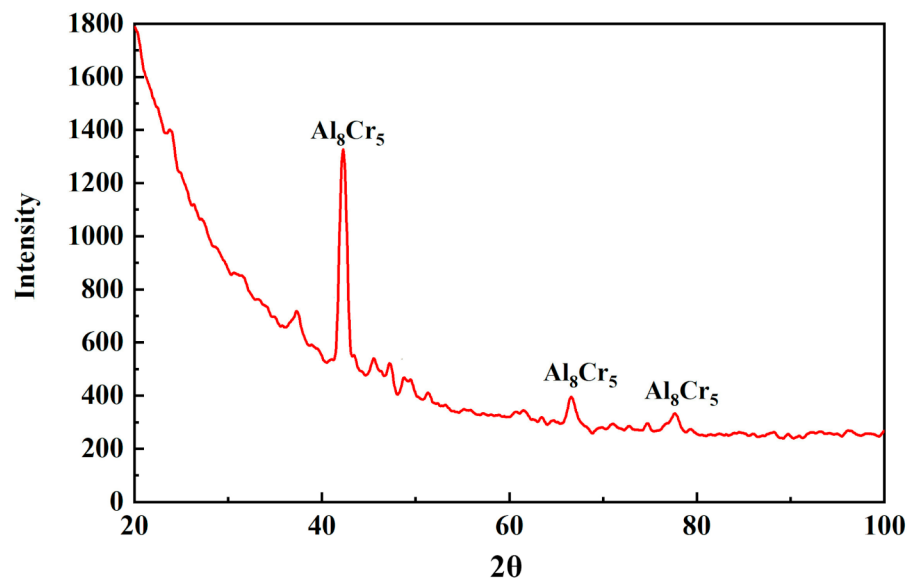


Figure 6. The GIXRD patterns of the surface of the Cr-Al diffusion coating.

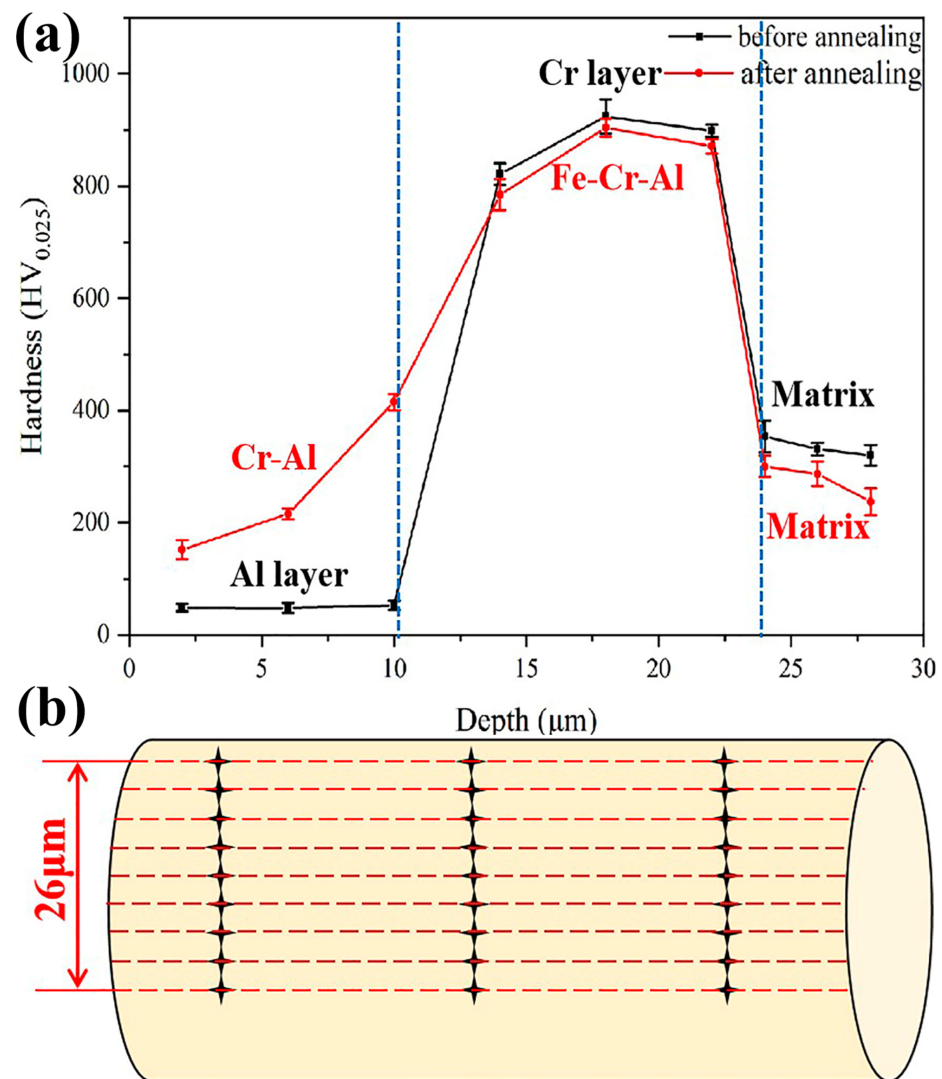


Figure 7. (a) The hardness of Cr-Al coating before and after annealing, and (b) the test points of the Vickers hardness.

3.2. Cross-Sectional Microstructures after Corrosion

The cross-sectional SEM image of the uncoated sample after LBE corrosion is shown in Figure 8. Dissolution and oxidation corrosion occurred in the uncoated sample, as shown in Figure 8a. The LBE permeated the uncoated sample via its boundaries, and the maximum depth reached 225 μm after corrosion for 1000 h. It can also be clearly observed that a thin oxide layer was produced on the 304 tube. Moreover, as shown in the mapping images in Figure 8b, a double oxide layer was found. In the case of the austenitic steels, the oxide layer included an outer Fe₃O₄ layer and an inner Fe-Cr spinel layer [33]. In order to explore the distribution of the interface elements after lead–bismuth corrosion, EDS point scans were performed on the double oxide layer in Figure 8b. As shown in Table 3, the outer oxide scale is rich in Fe and O, and its chemical composition (in at.%) is 41.92% Fe, 55.17% O and 2.91% Cr. The inner oxide layer is rich in Fe, Cr, Ni and O, and its chemical composition (in at.%) is 23.32% Fe, 21.20% Cr, 9.07% Ni and 46.41% O. From the atomic ratio of the chemical elements, it can be inferred that the outer layer is an Fe₃O₄ magnetite layer, and the inner layer is an Fe-Cr spinel layer. The inter-diffusion mechanism of the elements can be used to explain the formation of the double-layer oxide film [34]. First, an in-grown Fe-Cr spinel layer will be formed on the surface of the material. Once this thin spinel layer is produced, Fe ions diffuse from the substrate to the surface and combine with O on the surface to form Fe₃O₄, which grows from the original surface of the steel. Therefore, the continuous

inter-diffusion behavior of O and Fe ions at the corrosion interface is the main reason for the formation of the double-layer oxide film [35]. In addition, some cracks through the oxide layer were found due to thermal pressing, which provided an infiltration channel for the diffusion of molten LBE into the matrix.

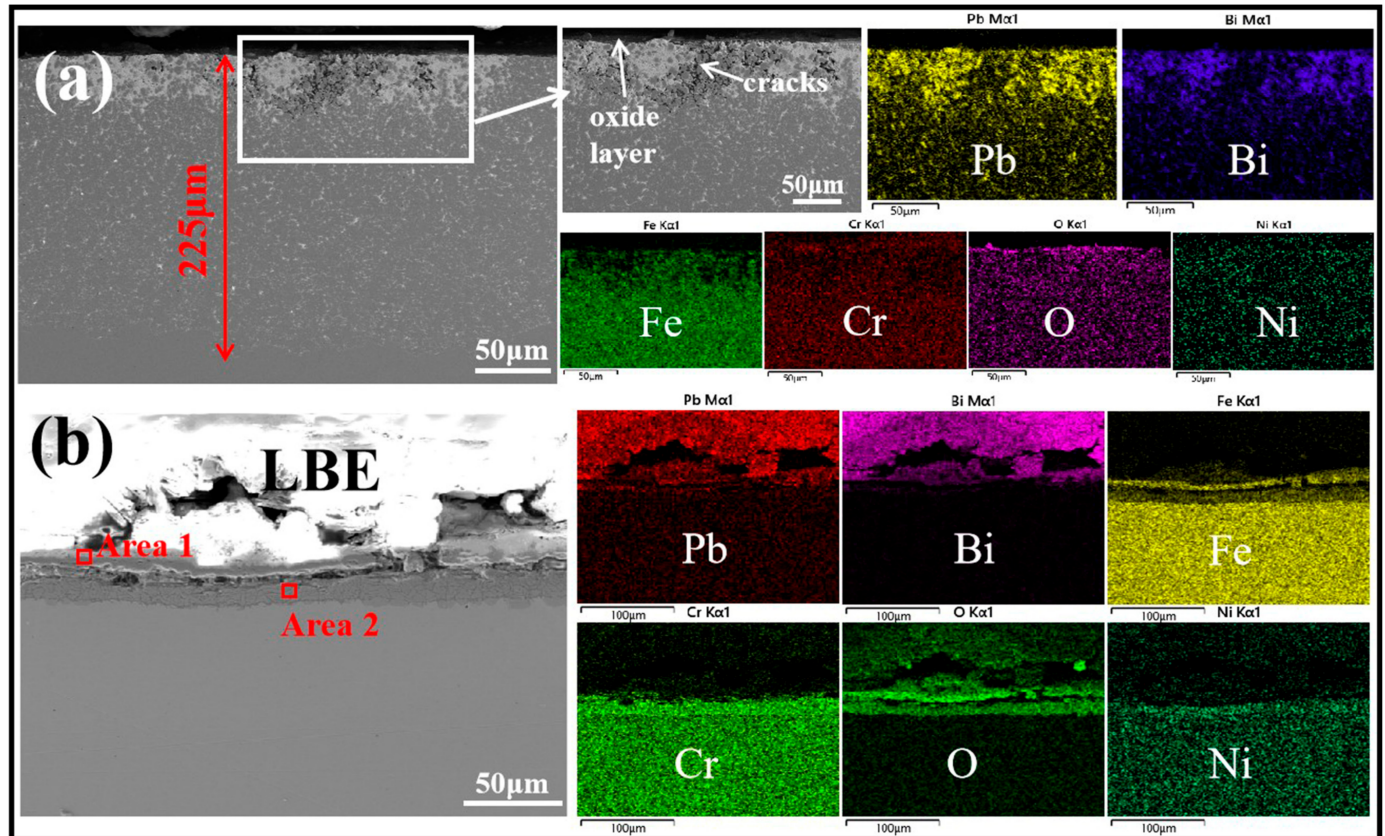


Figure 8. Cross-sectional microstructure and the element distribution for the uncoated sample after LBE corrosion, as given by EDS mapping analysis: (a) dissolution and oxidation corrosion; (b) oxidation corrosion.

Table 3. SEM-EDS results of the chemical compositions (at.%) of the marked micro-regions in Figure 8.

Area	O	Fe	Cr	Ni
1	55.17	41.92	2.91	0
2	46.41	23.32	21.20	9.07

Figure 9 shows the cross-sectional SEM and corresponding EDS mapping images of an annealed Cr-Al-coated sample after LBE corrosion at 600 °C. For the Cr-Al diffusion coating, the uniform structure can still be retained after LBE corrosion for 1000 h, and no cracks or holes can be found. Meanwhile, an oxide layer was formed at the interface of the LBE and the surface of the Cr-Al diffusion coating after LBE corrosion. The results show that Cr-Al diffusion coating provides good oxidation resistance because of the formation of the oxide layer, which blocks oxygen's inward diffusion into the matrix and effectively prevents the LBE entering the matrix. Thus, the Pb and Bi elements can be effectively limited to the upper side of the coating in Figure 9, indicating the good LBE corrosion resistance of the Cr-Al diffusion coating.

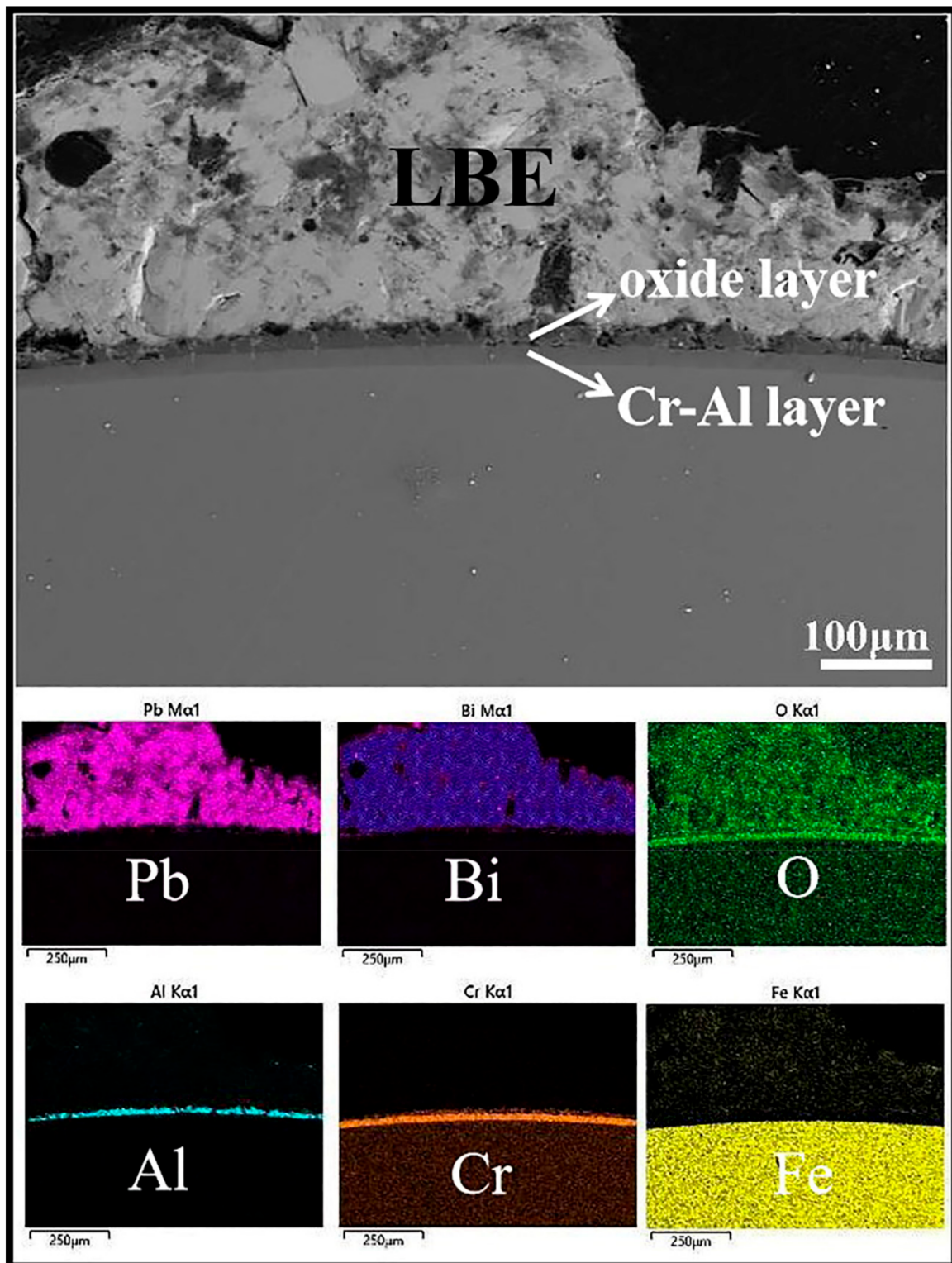


Figure 9. Cross-sectional microstructure and the element distribution for annealed Cr-Al-coated sample after LBE corrosion by EDS mapping analysis.

3.3. Surface Microstructures before and after Corrosion

Figure 10 shows the surface SEM images of the uncoated sample and the annealed Cr-Al-coated sample before and after LBE corrosion at 600 °C. There were a few submicron droplets on the surface of the original sample in Figure 10a, which was flat and smooth. However, the surface of the corroded sample was rough, with some cracks, as shown in

Figure 10b. After the cleaning of the solid LBE, streaky corrosion traces were observed on the surface, indicating that the uncoated sample was dissolved by liquid LBE. As shown in Figure 10c, the Cr-Al diffusion coating exhibited a relatively smooth and dense morphology. After corrosion at 600 °C, a small amount of pellets could be observed on the coating's surface in Figure 10d. The chemical compositions of the uncoated sample after corrosion and the annealed Cr-Al-coated sample before and after corrosion are both presented in Table 4. The chemical composition (in at.%) of the oxygen content was 43.69% in the uncoated sample after corrosion in area 1, indicating that the surface of the uncoated 304 tube was significantly oxidized at 600 °C. The chemical composition (in at.%) of the Fe content and Cr content were 21.95% and 28.44%, respectively, in the surface of the uncoated 304 tube at the same time, further proving that the surface corrosion products of uncoated 304 after LBE corrosion at 600 °C are magnetite and Fe-Cr spinel. Combining areas 2 and 3, 25.65% of the O content can be detected from the surface of the Cr-Al diffusion coating. However, the chemical composition (in at.%) of the O content is 41.76% in the coating after the corrosion test. Simultaneously, the Al content was reduced from 46.01 at.% to 11.17 at.%. It was also reported that the Al in the surface layer with high Al concentrations will dissolve into liquid LBE [36]. The Cr content increased from 24.19 at.% to 46.13 at.% due to the decrease of the Al content. The results revealed that the surface Cr-Al layer had been oxidized after LBE corrosion.

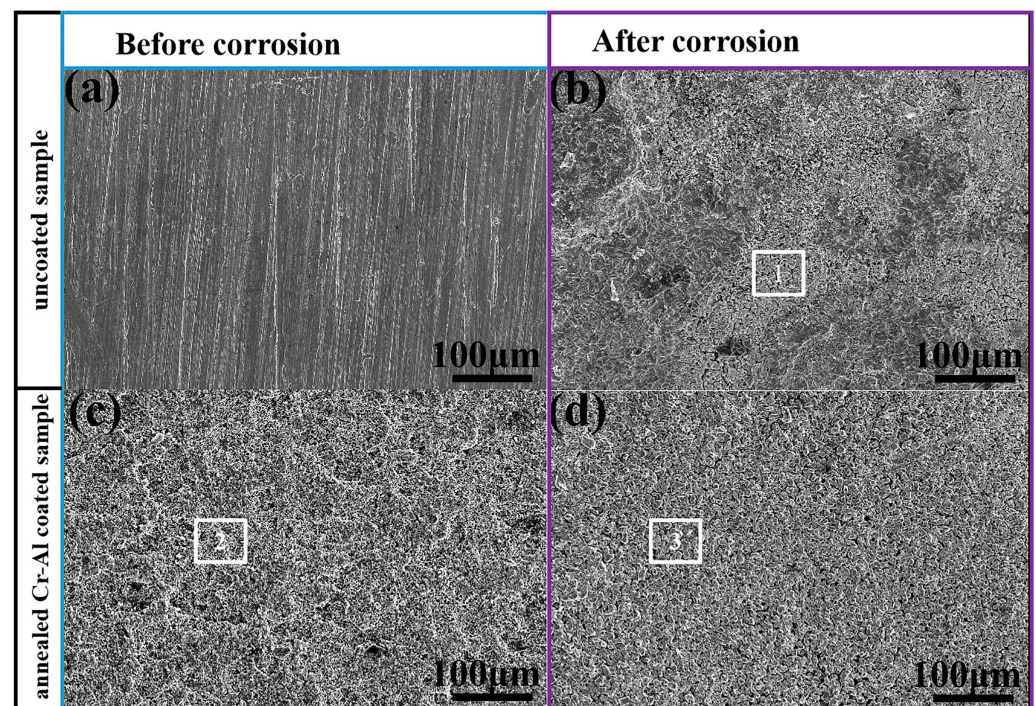


Figure 10. Surface SEM images of the uncoated sample (a) before and (b) after LBE corrosion at 600 °C. Surface SEM images of the annealed Cr-Al-coated sample (c) before and (d) after LBE corrosion at 600 °C (the LBE was removed).

Table 4. SEM-EDS results of the chemical compositions (at.%) of the marked micro-regions in Figure 10.

Area	O	Fe	Cr	Ni	Al
1	43.69	21.95	28.44	5.92	0
2	25.65	3.20	24.19	0.95	46.01
3	41.76	0.94	46.13	0	11.17

In order to explore the chemical composition of the oxide layer on the surface of the uncoated sample and the annealed Cr-Al-coated sample after LBE corrosion, the corresponding XPS Fe 2p, Al 2p, Cr 2p and O 1s spectra were employed, as shown in Figure 11. For the uncoated sample, the XPS spectra of Fe 2p in Figure 11a was deconvoluted into two peaks at 710.3 eV and 714.5 eV, respectively, corresponding to FeCr_2O_4 and Fe_3O_4 [37]. At the same time, the Cr 2p peak at 577 eV appeared in Figure 11b, which corresponds to the typical peak of FeCr_2O_4 [37]. The results proved that the oxide layer on the surface of the uncoated sample mainly consists of Fe_3O_4 and FeCr_2O_4 after LBE corrosion. The XPS spectra of O 1s in Figure 11c can be resolved into near-surface oxygen and chemisorption oxygen centered at 532.2 eV, which is labeled O_{ads} [38]. O_{ads} have been shown to be the main reactive oxygen species in oxidation reactions [39], which are considered to be essential for the formation of oxides.

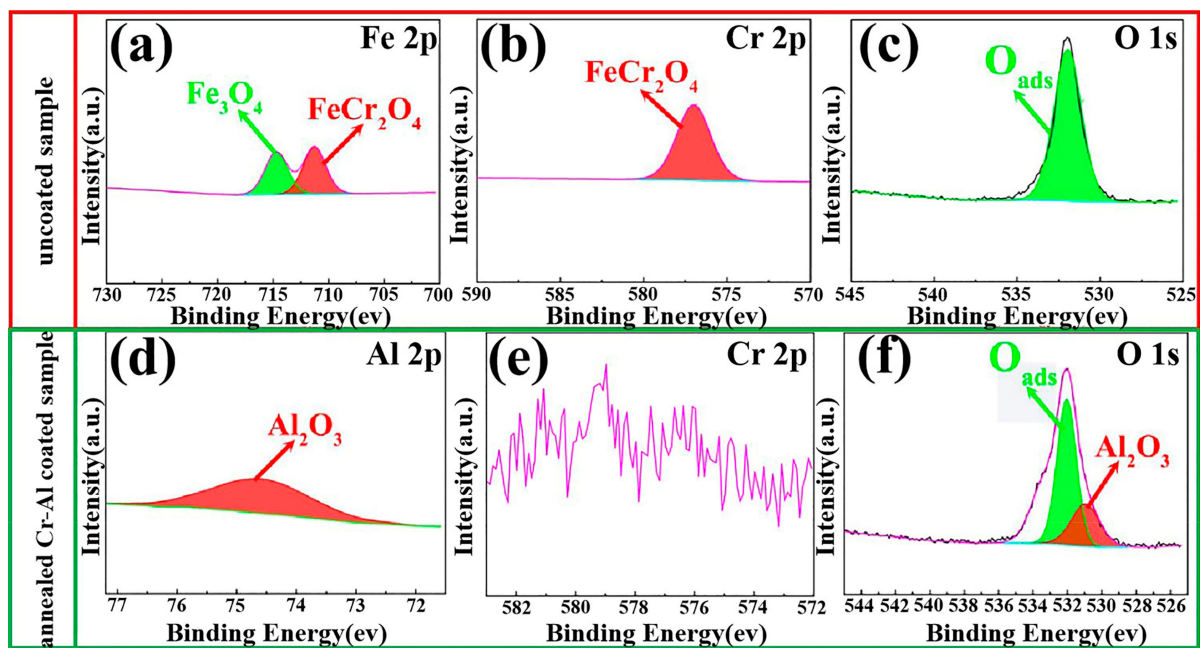


Figure 11. Surface XPS analysis of the uncoated sample and the annealed Cr-Al-coated sample after LBE corrosion: (a) Fe 2p (b) Cr 2p, and (c) O 1s XPS spectra of the uncoated sample; (d) Al 2p (e) Cr 2p, and (f) O1s XPS spectra of the annealed Cr-Al-coated sample.

Figure 11d shows the XPS spectra of Al 2p for the annealed Cr-Al-coated sample; a peak was found at 73.4 eV, which was assigned to Al_2O_3 [40]. As shown in Figure 11e, there were almost no peaks of Cr 2p. Furthermore, O_{ads} could be observed from the peak of O 1s in Figure 11f. The XPS results suggested that the oxide layer on the surface of the Cr-Al diffusion coating after LBE corrosion mainly consists of Al_2O_3 .

4. Conclusions

In this paper, a Cr-Al coating was deposited onto stainless steel 304 through MAIP Cr and MAIP Al; we then put the Cr-Al-coated sample into a resistance furnace for annealing treatment at a temperature of 600 °C for 12 h. The uncoated sample and the annealed Cr-Al-coated sample were exposed to LBE corrosion at 600 °C for 1000 h. The main results are as follows:

- (1) The main phase for the surface of the Cr-Al coating after annealing was Al_8Cr_5 . The annealed Cr-Al diffusion coating exhibited an average hardness of 260 HV, which is about five times as high as that of the Al coating before annealing, of which the average hardness was 48 HV.

- (2) The uncoated sample was corroded by the dissolution and oxidation of LBE severely. The surface of the 304 stainless steel produced an outer magnetite layer of Fe_3O_4 and an inner spinel layer of FeCr_2O_4 after LBE corrosion.
- (3) The annealed MAIP Cr-Al coating is being considered as a potential candidate for the improvement of the LBE corrosion resistance of the structural materials in an LBE-cooled nuclear reactor, as it retained its integrity without defects after LBE corrosion.
- (4) The favorable corrosion resistance can be attributed to the formation of the oxide layer, which mainly consisted of Al_2O_3 on the coating surface, as was detected by XPS.

In this study, a Cr layer was prepared by multi-arc ion plating between stainless steel 304 and the Al coating, and the Cr-Al alloy layer was obtained by vacuum diffusion on the surface of stainless steel 304, which could be a possible way to solve the hidden dangers that the pure Al coating is too soft and falls off too easily in the flowing LBE. Furthermore, the method simply improves the ability of the structural material to form a protective oxide layer in LBE.

Author Contributions: W.S.: conceptualization, methodology, formal analysis, writing—original draft. Z.T.: supervision, writing—review and editing. J.W.: project administration. G.C.: data curation. W.Y.: visualization. H.Z.: resources. All authors have read and agreed to the published version of the manuscript.

Funding: This research received no external funding.

Institutional Review Board Statement: Not applicable.

Informed Consent Statement: Not applicable.

Data Availability Statement: Data available in a publicly accessible repository.

Acknowledgments: The authors gratefully acknowledge the foundation of grants provided by the lead and bismuth reactor R&D team of Chengdu Nuclear Power Research Institute, Sichuan Province.

Conflicts of Interest: The authors declare that they have no known competing financial interests or personal relationships that could have appeared to influence the work reported in this paper.

References

1. Gong, X.; Chen, J.; Hu, F.; Xiang, C.; Yu, Z.; Xiao, J.; Wang, H.; Gong, H.; Wang, H.; Liu, C.; et al. Liquid metal embrittlement of an Fe10Cr4Al ferritic alloy exposed to oxygen-depleted and -saturated lead-bismuth eutectic at 350 °C. *Corros. Sci.* **2020**, *165*, 108364. [[CrossRef](#)]
2. Lambrinou, K.; Charalampopoulou, E.; Van der Donck, T.; Delville, R.; Schryvers, D. Dissolution corrosion of 316L austenitic stainless steels in contact with static liquid lead-bismuth eutectic (LBE) at 500 °C. *J. Nucl. Mater.* **2017**, *490*, 9–27. [[CrossRef](#)]
3. Yang, J.; Shi, K.; Zhang, W.; Chen, Q.; Ning, Z.; Zhu, C.; Liao, J.; Yang, Y.; Liu, N.; Yang, J. A novel AlCrFeMoTi high-entropy alloy coating with a high corrosion-resistance in lead-bismuth eutectic alloy. *Corros. Sci.* **2021**, *187*, 109524. [[CrossRef](#)]
4. Chen, G.; Ju, N.; Lei, Y.; Wang, D.; Zhu, Q.; Li, T. Corrosion behavior of base metal and weld bead of CLAM steel in flowing Pb-Bi at 550 °C. *Prog. Nucl. Energy* **2020**, *118*, 103074. [[CrossRef](#)]
5. Yao, C.; Zhang, H.; Chang, H.; Sheng, Y.; Shen, T.; Zhu, Y.; Pang, L.; Cui, M.; Wei, K.; Xu, Y.; et al. Structure of surface oxides on martensitic steel under simultaneous ion irradiation and molten LBE corrosion. *Corros. Sci.* **2022**, *195*, 109953. [[CrossRef](#)]
6. Wan, Q.; Wu, Z.; Liu, Y.; Yang, B.; Liu, H.; Ren, F.; Wang, P.; Xiao, Y.; Zhang, J.; Zhang, G. Lead-bismuth eutectic (LBE) corrosion mechanism of nano-amorphous composite TiSiN coatings synthesized by cathodic arc ion plating. *Corros. Sci.* **2021**, *183*, 109264. [[CrossRef](#)]
7. Wang, Q.-M.; Cheng, X.-M.; Li, Y.-Y.; Yu, G.-M.; Liu, Z. High-temperature corrosion of Sn-Bi-Zn-Ga alloys as heat transfer fluid. *Rare Met.* **2020**, *40*, 2221–2229. [[CrossRef](#)]
8. Stergar, E.; Eremin, S.; Gavrilov, S.; Lambrecht, M.; Makarov, O.; Iakovlev, V. Influence of LBE long term exposure and simultaneous fast neutron irradiation on the mechanical properties of T91 and 316L. *J. Nucl. Mater.* **2016**, *473*, 28–34. [[CrossRef](#)]
9. Baker, B.; Brewer, L. Evaluation of liquid metal embrittlement susceptibility of oxide dispersion strengthened steel MA956. *J. Nucl. Mater.* **2014**, *453*, 239–246. [[CrossRef](#)]
10. Huang, X.; Gong, X.; Song, M.; Chen, J.; Hu, F.; Yin, Y.; Xiao, J.; Wang, H.; Wang, H.; Gong, H.; et al. Liquid metal embrittlement susceptibility of a high-entropy alloy exposed to oxygen-depleted liquid lead-bismuth eutectic at 250 and 350 °C. *J. Nucl. Mater.* **2020**, *528*, 151859. [[CrossRef](#)]
11. Bahrami, A.; Anijdan, S.M.; Taheri, P.; Mehr, M.Y. Failure of AISI 304H stainless steel elbows in a heat exchanger. *Eng. Fail. Anal.* **2018**, *90*, 397–403. [[CrossRef](#)]

12. Anijdan, S.M.; Sabzi, M.; Ghobeiti-Hasab, M.; Roshan-Ghiyas, A. Optimization of spot welding process parameters in dissimilar joint of dual phase steel DP600 and AISI 304 stainless steel to achieve the highest level of shear-tensile strength. *Mater. Sci. Eng. A* **2018**, *726*, 120–125. [[CrossRef](#)]
13. Saffari, H.; Shamanian, M.; Bahrami, A.; Szpunar, J.A. Effects of ERNiCr-3 butter layer on the microstructure and mechanical properties of API 5L X65/AISI304 dissimilar joint. *J. Manuf. Process.* **2020**, *50*, 305–318. [[CrossRef](#)]
14. Ferré, F.G.; Mairov, A.; Iadicco, D.; Vanazzi, M.; Bassini, S.; Utili, M.; Tarantino, M.; Bragaglia, M.; Lamastra, F.; Nanni, F.; et al. Corrosion and radiation resistant nanoceramic coatings for lead fast reactors. *Corros. Sci.* **2017**, *124*, 80–92. [[CrossRef](#)]
15. Chen, Y.; Hu, L.; Qiu, C.; He, B.; Zhou, L.; Zhao, J.; Li, Y. Influence of LBE Temperatures on the Microstructure and Properties of Crystalline and Amorphous Multiphase Ceramic Coatings. *Coatings* **2019**, *9*, 543. [[CrossRef](#)]
16. Niu, R.; Li, J.; Wang, Y.; Chen, J.; Xue, Q. Structure and high temperature tribological behavior of TiAlN/nitride duplex treated coatings on Ti6Al4V. *Surf. Coat. Technol.* **2017**, *309*, 232–241. [[CrossRef](#)]
17. Ferré, F.G.; Ormellesse, M.; Di Fonzo, F.; Beghi, M. Advanced Al₂O₃ coatings for high temperature operation of steels in heavy liquid metals: A preliminary study. *Corros. Sci.* **2013**, *77*, 375–378. [[CrossRef](#)]
18. Miorin, E.; Montagner, F.; Zin, V.; Giuranno, D.; Ricci, E.; Pedroni, M.; Spampinato, V.; Vassallo, E.; Deambrosis, S.M. Al rich PVD protective coatings: A promising approach to prevent T91 steel corrosion in stagnant liquid lead. *Surf. Coat. Technol.* **2019**, *377*, 124890. [[CrossRef](#)]
19. Wu, Z.; Zhao, X.; Liu, Y.; Cai, Y.; Li, J.; Chen, H.; Wan, Q.; Yang, D.; Tan, J.; Liu, H.; et al. Lead-bismuth eutectic (LBE) corrosion behavior of AlTiN coatings at 550 and 600 °C. *J. Nucl. Mater.* **2020**, *539*, 152280. [[CrossRef](#)]
20. Charalampopoulou, E.; Lambrinou, K.; Van der Donck, T.; Paladino, B.; Di Fonzo, F.; Azina, C.; Eklund, P.; Mráz, S.; Schneider, J.M.; Schryvers, D.; et al. Early stages of dissolution corrosion in 316L and DIN 1.4970 austenitic stainless steels with and without anticorrosion coatings in static liquid lead-bismuth eutectic (LBE) at 500 °C. *Mater. Charact.* **2021**, *178*, 111234. [[CrossRef](#)]
21. Daure, J.; Carrington, M.; Shipway, P.; McCartney, D.; Stewart, D. A comparison of the galling wear behaviour of PVD Cr and electroplated hard Cr thin films. *Surf. Coat. Technol.* **2018**, *350*, 40–47. [[CrossRef](#)]
22. Liang, A.; Li, Y.; Liang, H.; Ni, L.; Zhang, J. A favorable chromium coating electrodeposited from Cr(III) electrolyte reveals anti-wear performance similar to conventional hard chromium. *Mater. Lett.* **2017**, *189*, 221–224. [[CrossRef](#)]
23. Bikulcius, G.; Češunienė, A.; Selskienė, A.; Pakštas, V.; Matijošius, T. Dry sliding tribological behavior of Cr coatings electrodeposited in trivalent chromium sulphate baths. *Surf. Coat. Technol.* **2017**, *315*, 130–138. [[CrossRef](#)]
24. Peng, B.; Li, H.; Zhang, Q.; Xu, Y.X.; Wei, T.; Wang, Q.; Zhang, F.; Kim, K.H. High-temperature thermal stability and oxidation resistance of Cr and Ta co-alloyed Ti—Al—N coatings deposited by cathodic arc evaporation. *Corros. Sci.* **2020**, *167*, 108490. [[CrossRef](#)]
25. Wulf, S.-E.; Krauss, W.; Konys, J. Long-term corrosion behavior of Al-based coatings in flowing Pb–15.7Li, produced by electrochemical ECX process. *Nucl. Mater. Energy* **2018**, *16*, 158–162. [[CrossRef](#)]
26. He, J.; Liao, X.; Lan, X.; Qiu, W.; Yu, H.; Zhang, J.; Fan, W.; Zhong, X.; Liu, Z. Annealed Al-Cr coating: A hard anti-corrosion coating with grain boundary modification effect for Nd-Fe-B magnets. *J. Alloys Compd.* **2021**, *870*, 159229. [[CrossRef](#)]
27. Zhou, S.; Kuang, T.; Qiu, Z.; Zeng, D.; Zhou, K. Microstructural origins of high hardness and toughness in cathodic arc evaporated Cr-Al-N coatings. *Appl. Surf. Sci.* **2019**, *493*, 1067–1073. [[CrossRef](#)]
28. Sharma, R.K.; Das, R.K.; Kumar, S.R. Effect of chromium content on microstructure, mechanical and erosion properties of Fe-Cr-Ti-Mo-C-Si coating. *Surf. Interfaces* **2021**, *22*, 100820. [[CrossRef](#)]
29. Park, J.-H.; Kim, H.-G.; Park, J.-Y.; Jung, Y.-I.; Park, D.-J.; Koo, Y.-H. High temperature steam-oxidation behavior of arc ion plated Cr coatings for accident tolerant fuel claddings. *Surf. Coat. Technol.* **2015**, *280*, 256–259. [[CrossRef](#)]
30. Ma, X.-F.; Wu, Y.-W.; Tan, J.; Meng, C.-Y.; Yang, L.; Dang, W.-A.; He, X.-J. Evaluation of corrosion and oxidation behaviors of TiAlCrN coatings for nuclear fuel cladding. *Surf. Coat. Technol.* **2019**, *358*, 521–530. [[CrossRef](#)]
31. Chen, G.; Wang, J.; Zhang, H.; Li, L.; Fan, H. Low-temperature oxy-nitriding of 316 L austenitic stainless steel for improved corrosion resistance in liquid lead-bismuth eutectic. *Scr. Mater.* **2021**, *202*, 114014. [[CrossRef](#)]
32. Cionea, C.; Abad, M.D.; Aussat, Y.; Frazer, D.; Gubser, A.; Hosemann, P. Oxide scale formation on 316L and FeCrAl steels exposed to oxygen controlled static LBE at temperatures up to 800 °C. *Sol. Energy Mater. Sol. Cells* **2016**, *144*, 235–246. [[CrossRef](#)]
33. Sapundjiev, D.; Van Dyck, S.; Bogaerts, W. Liquid metal corrosion of T91 and A316L materials in Pb–Bi eutectic at temperatures 400–600 °C. *Corros. Sci.* **2006**, *48*, 577–594. [[CrossRef](#)]
34. Aiello, A.; Azzati, M.; Benamati, G.; Gessi, A.; Long, B.; Scaddozzo, G. Corrosion behaviour of stainless steels in flowing LBE at low and high oxygen concentration. *J. Nucl. Mater.* **2004**, *335*, 169–173. [[CrossRef](#)]
35. Müller, G.; Schumacher, G.; Zimmermann, F. Investigation on oxygen controlled liquid lead corrosion of surface treated steels. *J. Nucl. Mater.* **2000**, *278*, 85–95. [[CrossRef](#)]
36. Kurata, Y.; Sato, H.; Yokota, H.; Suzuki, T. Applicability of Al-Powder-Alloy Coating to Corrosion Barriers of 316SS in Liquid Lead-Bismuth Eutectic. *Mater. Trans.* **2011**, *52*, 1033–1040. [[CrossRef](#)]
37. Biesinger, M.C.; Payne, B.P.; Grosvenor, A.P.; Lau, L.W.M.; Gerson, A.R.; Smart, R.S.C. Resolving surface chemical states in XPS analysis of first row transition metals, oxides and hydroxides: Cr, Mn, Fe, Co and Ni. *Appl. Surf. Sci.* **2011**, *257*, 2717–2730. [[CrossRef](#)]
38. Chen, G.; Xue, L.; Wang, J.; Tang, Z.; Li, X.; Dong, H. Investigation of surface modifications for combating the molten aluminum corrosion of AISI H13 steel. *Corros. Sci.* **2020**, *174*, 108836. [[CrossRef](#)]

39. Simmons, J.W.; Atteridge, D.G.; Rawers, J.C. Sensitization of High-Nitrogen Austenitic Stainless Steels by Dichromium Nitride Precipitation. *Corrosion* **1994**, *50*, 491–501. [[CrossRef](#)]
40. Tago, T.; Kataoka, N.; Tanaka, H.; Kinoshita, K.; Kishida, S. XPS study from a clean surface of Al₂O₃ single crystals. *Procedia Eng.* **2017**, *216*, 175–181. [[CrossRef](#)]